Research Square

Preprints are preliminary reports that have not undergone peer review.
They should not be considered conclusive, used to inform clinical practice,
or referenced by the media as validated information.

Microwave dielectric properties and chemical bond characteristics of Sr2+ /Nd3+ co-substituted CaSm 2 (MoO4)4 low- temperature sintered ceramics for LTCC applications

Xiuyuan Su
Zhaoqing University
Haiqing Gan
Zhaoqing University
Haiqiang Lin
Zhaoqing University
Shijie Ma
Zhaoqing University
Jiahui Li
Zhaoqing University
Zhiyong Xu
Zhaoqing University
Yukuai Liu
liuyukuai@zqu.edu.cn

Zhaoqing University

Research Article

Keywords: Molybdate ceramic, Microwave dielectric property, LTCC, P-V-L theory

Posted Date: November 24th, 2026

DOI: https://doi.org/10.21203/rs.3.rs-11686041/v1

License: This work is licensed under a Creative Commons Attribution 4.0 International License.
Read Full License

Additional Declarations: No competing interests reported.

Microwave dielectric properties and chemical bond characteristics of Sr^{2+}/Nd^{3+} co-substituted $CaSm_2(MoO_4)_4$ low-temperature sintered ceramics for LTCC applications

Xiuyuan Su, Haiqing Gan, Haiqiang Lin, Shijie Ma, Jiahui Li, Zhiyong Xu and Yukuai Liu*

School of Electronics and Electrical Engineering, Zhaoqing University, Guangdong, PR China, 526061

Abstract

In this work, Sr^{2+} and Nd^{3+} ions were employed to co-substitute Ca^{2+} and Sm^{3+} in $CaSm_2(MoO_4)_4$ ceramics to tailor their microwave dielectric properties for LTCC applications. The co-substitution maintains a single-phase tetragonal scheelite-type solid solution and reduces the optimum sintering temperature from 1000℃ for the parent to 950℃, approaching the temperature window required for Ag-based LTCC co-firing, while markedly improving the Q×f value. The Q×f enhancement is attributed mainly to improved densification, which suppresses porosity-related dielectric loss, together with a genuine intrinsic contribution from enhanced cation ordering, as evidenced by the narrowing of the Raman FWHM of the $[MoO_4]$ A_g mode. The relative permittivity decreases slightly with x(x=0.02-0.11), governed primarily by the expansion of the unit cell, which dilutes the polarizability density, and is further modulated by the relative density. On the basis of the P–V–L bond theory, the Ca/Sm–O bonds exhibit the highest ionicity and thus dominate the permittivity contribution, whereas the strong Mo–O bonds with the largest lattice and bond energies stabilize the crystal framework; the derived thermal expansion coefficient α correlates with the temperature stability of τf. Notably, the $Ca_{1-x}Sr_xSm_{2-x}Nd_x(MoO_4)_4$(x=0.08) ceramic sintered at 950 °C exhibits optimal dielectric properties of εr = 11.788 ± 0.071, Q×f = 85,324 ± 3885 GHz and τ_f = −43.94 ppm/℃. The combination of low-temperature sinterability and high Q×f renders this series a promising candidate for LTCC applications.

Keywords：Molybdate ceramic ; Microwave dielectric property ; LTCC ; P-V-L theory

Corresponding authors' e-mail: liuyukuai@zqu.edu.cn.

1.Introduction

The rapid advancement of communication technologies is profoundly driving technological innovation and economic growth[1-2]. As the cornerstone of next-generation information technology, 5G systems are being deployed on a large scale worldwide, while research and development on 6G technology have also been initiated, propelling communication technologies toward higher frequency bands, higher data transmission rates and lower latency. With the booming development of communication technologies, microwave dielectric ceramics have become the dominant materials for filters, resonators, capacitors and substrates, and serve as an indispensable component in human digital life[3-5] Especially in the 5G/6G era, millimetre-wave bands will witness increasingly extensive applications, which impose ever-stringent requirements on the dielectric properties of microwave dielectric ceramics[6-8]. Materials with low relative permittivity help reduce the signal delay during the transmission of high-frequency electromagnetic waves[9-11], and such feature can significantly improve data transmission rates. Currently, driven by technological innovations in the electronic information industry, low-temperature co-fired ceramic (LTCC) materials simultaneously possessing high-frequency performance and low dielectric loss are in urgent demand. Relevant investigations have evolved into a core research hotspot within the field of microwave dielectric ceramics.

As a category of advanced integration technology, LTCC not only fully inherits the technological and performance merits of high-temperature co-fired ceramics (HTCC), but also integrates the flexible adaptability of thick-film technology. It exhibits irreplaceable application potential in the miniaturization, integration, high-frequency operation and multi-functional integration of electronic components[3][12]. In addition, ceramic components with low sintering temperatures possess distinct advantages in mass production: they can cut manufacturing costs, improve energy efficiency and reduce carbon emissions, which is fully consistent with the concept of sustainable green manufacturing. Accordingly, realizing the low-temperature sintering of ceramic materials while guaranteeing favourable microwave dielectric properties has become a critical scientific issue that urgently needs to be addressed in this field[13].

In recent years, numerous molybdate-based ceramics with outstanding comprehensive properties and low sintering temperatures have attracted considerable research interest, and relevant

achievements are summarized in **Table 1**. As a family of novel low-melting-point compounds, molybdenum-based ceramics have received extensive attention in the field of microwave materials[14-15]. Among them, oxide systems with silica-type structural characteristics (A = Ca, Sr, Ba, etc.) exhibit excellent microwave dielectric properties, rendering them highly suitable for LTCC applications. Against this backdrop, ceramics with the general formula $ALn_2(MoO_4)_4$ (where A denotes divalent alkaline-earth metal ions and Ln represents trivalent rare-earth ions) have aroused widespread concern. On the basis of systematic investigations on ternary systems, Zhao et al. reported a novel $CaSm_2(MoO_4)_4$ ceramic[16]. The sintering temperature of the parent ceramic clearly exceeds the tolerance of Ag-based LTCC processing, which restricts its practical use in LTCC modules.

In this work, the dielectric properties of $CaSm_2(MoO_4)_4$ ceramic with Ca^{2+} and Sm^{3+} ions substituted by Sr^{2+} and Nd^{3+} ions are studied, due to whose ionic radii are close to those of Ca^{2+} and Sm^{3+}. Sr^{2+} and Nd^{3+} were selected because their ionic radii (1.13 Å for Sr^{2+} and 0.995 Å for Nd^{3+}) are comparable to those of the host Ca^{2+} (0.99 Å) and Sm^{3+} (0.964 Å), which favours the formation of a single-phase scheelite-type solid solution; moreover, the slightly larger substituting ions enlarge the unit cell and dilute the polarizability density, thereby lowering the relative permittivity, while the co-substitution effectively reduces the optimum sintering temperature towards the temperature window required for Ag-based LTCC co-firing. Experimental results reveal that the introduced ionic substitution can effectively reduce the sintering temperature and further optimize the microwave dielectric properties of this ceramic system. Accordingly, we systematically investigate the microwave dielectric characteristics of $Ca_{1-x}Sr_xSm_{2-x}Nd_x(MoO_4)_4$ ceramics. Combined with packing fraction analysis and the P-V-L chemical bond theory, the intrinsic influence mechanisms of chemical bonding and crystal structure on the microwave dielectric performances are elaborated in depth.

Table 1

Microwave dielectric properties of some Mo-based ceramics.

Materials	ε_r	$Q\times f$ (GHz)	τ_f (ppm/°C)	S.T. (°C)	References
$MgTeMoO_6$	11.93	34,453	-82.0	660	[17]
$ZnTeMoO_6$	12.39	29,153	-87.0	650	[17]
$NaCaPr(MoO_3)_4$	10.78	57,726	-44.6	775	[18]
$Na_{0.5}Nd_{0.5}MoO_4$	10.50	19,605	-49.0	760	[19]

$Na_{0.48}La_{0.52}MoO_4$	8.86	61,378	-10.8	920	[20]
$CaNd_4(MoO_4)_3$	13.84	44,560	-43	1400	[21]
$SrMoO_4$	9.49	61,000	-67	1050	[22]
$BaSm_2(MoO_4)_4$	11.80	20,000	-34	960	[23]
$CaSm_2(MoO_4)_4$	11.71	70,089	-53	1000	[16]
$Ca_{0.92}Sr_{0.08}Sm_{1.92}Nd_{0.08}(MoO_4)_4$	11.78	85,324	-43.94	950	This work

2.Method and materials

$Ca_{1-x}Sr_xSm_{2-x}Nd_x(MoO_4)_4$ ceramics were fabricated via the conventional solid-state reaction method using high-purity $CaCO_3$ (99.9%,Aladdin), Sm_2O_3 (99.5%,Macklin), MoO_3 (99.9%,Aladdin), Nd_2O_3 (99.5%,Macklin) and $SrCO_3$ (99.9%,Aladdin) as raw materials. Firstly, the starting powders were weighed according to the stoichiometric ratios of various compositions and wet-ball-milled in anhydrous ethanol for 24h with zirconia milling media. Subsequently, the obtained slurry was dried in an oven at 80℃, followed by calcination at 850℃. In the third step, the calcined powders were milled again, and 8 wt% polyvinyl alcohol (PVA) was added as a binder for thorough homogenization. The mixed powders were uniaxially pressed into cylindrical green pellets with a diameter of 11 mm and a thickness of 5.5 mm under 650 MPa. Afterward, the green bodies were held at 500℃ for 2 h to remove the PVA binder. Finally, these pellets were sintered at temperatures ranging from 875℃ to 975℃ for 4 h.

The phase identification of $Ca_{1-x}Sr_xSm_{2-x}Nd_x(MoO_4)_4$ ceramic powders was performed on a Bruker X-ray diffractometer over the 2θ range of 10°–80°. The Rietveld refinement of XRD data was carried out using the GSAS-II software. The sintered specimens were polished with W0.25 (80,000 mesh) diamond polishing paste. After gold sputtering for 120s, the surface microstructures of samples were characterized by a scanning electron microscope (SEM, S-4800). The grain sizes were statistically evaluated using Image-J software based on SEM micrographs. Raman spectra were collected on a LabRAM HR Evolution spectrometer equipped with a He-Ne laser (λ = 514 nm) in the wavenumber range of 150 cm^{-1} to 1000 cm^{-1}. The microwave dielectric properties were measured via the Hakki–Coleman dielectric resonator method[24] using a vector network analyzer (Anritsu MS4647B, USA). The temperature coefficient of resonant frequency (τ_f) was calculated according to Equation (1):

$$\tau_{\mathrm{f}} = \frac{f_{T_2} - f_{T_1}}{f_{T_1}(T_2 - T_1)} (\mathrm{ppm/^{\circ}C}) \quad (1)$$

In the above formula, f_{T_1} and f_{T_2} represent the resonant frequencies of the sample at 85℃ and 25℃, respectively.

3.Results and discussion

Fig. 1(a) shows the XRD patterns of $Ca_{1-x}Sr_xSm_{2-x}Nd_x(MoO_4)_4$ ceramics. The diffraction peaks of all samples are highly consistent with the standard card of $CaLa_2(MoO_4)_4$ (PDF#96-722-0855), and no additional diffraction peaks are observed. This indicates that the synthesized $Ca_{1-x}Sr_xSm_{2-x}Nd_x(MoO_4)_4$ ceramics present a tetragonal scheelite-type structure with the space group of $I4_1/a$. To further explore the variations in crystal structure, the XRD data of $Ca_{1-x}Sr_xSm_{2-x}Nd_x(MoO_4)_4$ ceramic samples were refined by GSAS-II software. **Fig. 1(b)** displays the refined XRD pattern of $Ca_{0.92}Sr_{0.08}Sm_{1.92}Nd_{0.08}(MoO_4)_4$ ceramic. **Fig. 2** illustrates a schematic diagram of the unit cell structure of $Ca_{0.92}Sr_{0.08}Sm_{1.92}Nd_{0.08}(MoO_4)_4$ ceramics with the tetragonal scheelite arrangement. The structural parameters obtained from the refinement are listed in **Table 2**. The results verify reliability of the refinement data and excellent validity of the structural model, which further demonstrates that the $Ca_{1-x}Sr_xSm_{2-x}Nd_x(MoO_4)_4$ ceramics possess a tetragonal scheelite-type structure. The atomic coordinates, ion occupancy and Wyckoff positions of the ceramics are summarized in **Table 3**.

$Ca_{1-x}Sr_xSm_{2-x}Nd_x(MoO_4)_4$ ceramics are composed of Ca/SmO_8 polyhedra and MoO_4 tetrahedra. The A-site cations, Ca^{2+} and Sm^{3+}, are coordinated with eight oxygen ions, forming the Ca/SmO_8 polyhedra (CN=8). Within the Ca/SmO_8 Ca/SmO_8 polyhedra, two distinct sets of Ca/Sm-O bonds are present, each with four identical bond lengths. Two Ca/SmO_8 polyhedra are connected by shared edges. The B-site cation, Mo^{6+}, bonds with four oxygen ions to form the MoO_4 tetrahedra(CN =4). During the XRD test, the sine value of the diffraction angle θ is inversely proportional to the interplanar spacing d, and the unit cell parameters are closely related to the interplanar spacing. Therefore, the shift of diffraction peaks toward low angles indicates the increase of interplanar spacing of CSSNM ($Ca_{1-x}Sr_xSm_{2-x}Nd_x(MoO_4)_4$) ceramics, which is mainly attributed to the variation of ionic radii caused by the substitution of Sm by Nd and Ca by Sr.

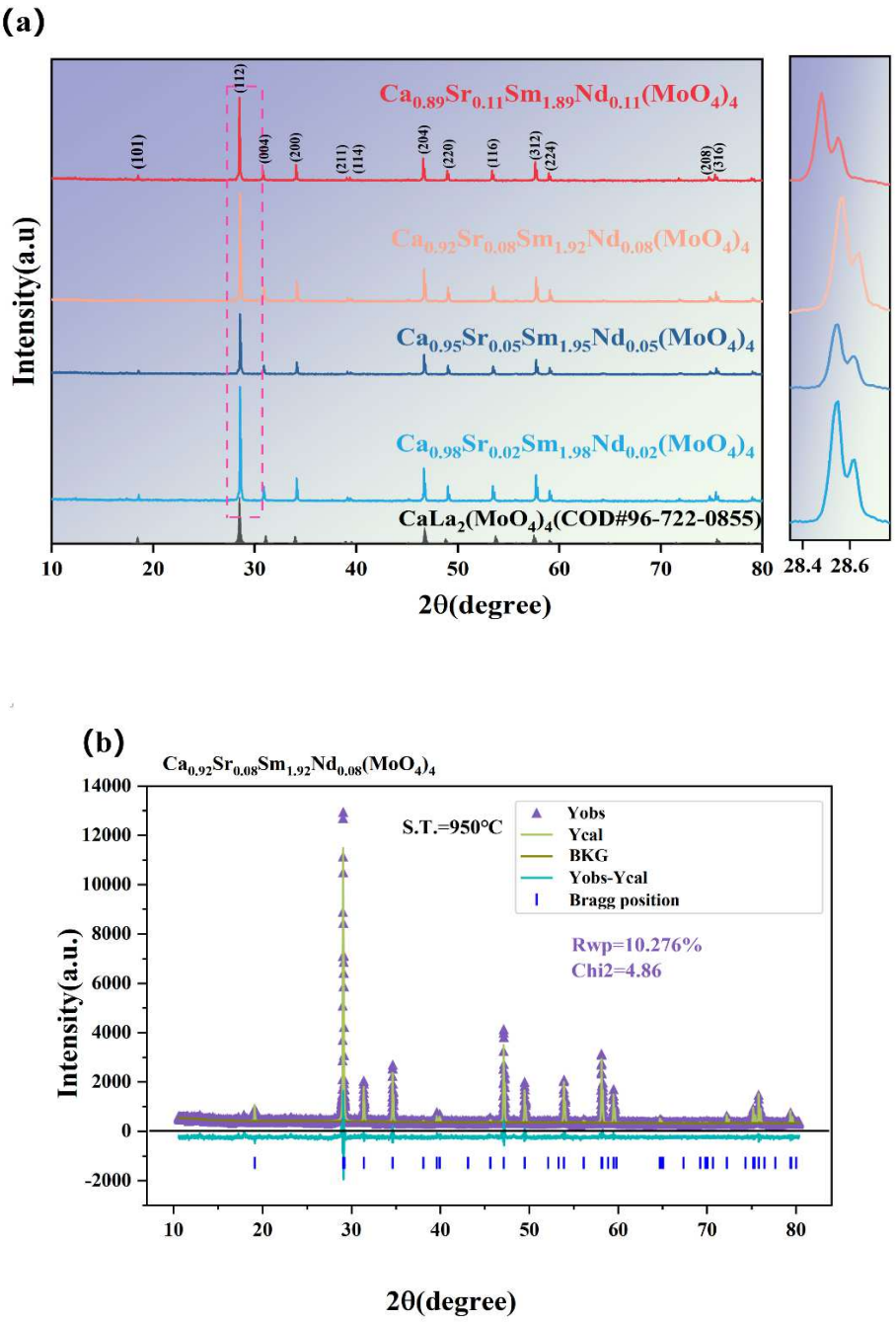


Fig. 1 (a) XRD patterns of CSSNM ceramics sintered at different x (substitution contents); **(b)** Rietveld refinement of CSSNM ceramic.

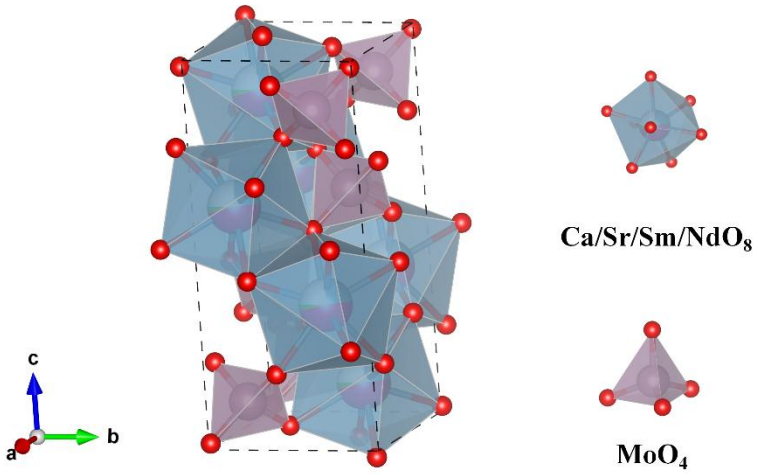


Fig. 2 Schematic diagram of the crystal structure of $Ca_{0.92}Sr_{0.08}Sm_{1.92}Nd_{0.08}(MoO_4)_4$ ceramics

Table 2

The Rietveld refinements of $Ca_{1-x}Sr_xSm_{2-x}Nd_x(MoO_4)_4$ (x denotes the substitution ratio) composite ceramics.

x	a=b(Å)	c(Å)	V(Å^3)	Rwp(%)	Chi2
0.02	5.24949	11.57111	318.866	9.588	3.94
0.05	5.25288	11.58042	319.535	10.130	3.79
0.08	5.25511	11.58858	320.032	10.276	4.86
0.11	5.25634	11.59375	320.324	10.154	4.05

Table 3

Fractional atomic coordinates (x, y, and z) of $Ca_{0.92}Sr_{0.08}Sm_{1.92}Nd_{0.08}(MoO_4)_4$ ceramics.

Atom	x	y	z	Occ.	Wyckoff
Ca	0	0.25	0.625	0.23	4b
Sm	0	0.25	0.625	0.48	4b
Nd	0	0.25	0.625	0.02	4b
Sr	0	0.25	0.625	0.02	4b
Mo	0	0.25	0.125	1	4a
O	0.23650	0.1023	0.04005	1	16f

Fig. 3 and **4** display the free-surface scanning electron microscope (SEM) micrographs and grain size variation of $Ca_{0.92}Sr_{0.08}Sm_{1.92}Nd_{0.08}(MoO_4)_4$ ceramics sintered at different temperatures. **Fig. 3(a–e)** present the SEM images of the ceramics sintered from 875 °C to 975 °C, while **Fig. 4(a–e)** illustrate the evolutionary trend of grain size with increasing sintering temperature. **Fig. 4(f)** shows the average grain curve of ceramics. It is observed that a small amount of pores appear on

the surface of the $Ca_{0.92}Sr_{0.08}Sm_{1.92}Nd_{0.08}(MoO_4)_4$ ceramics at the initial sintering stage. As the sintering temperature increases, the surface porosity decreases, the grain size increases, and the relative density of the samples is improved correspondingly. Insufficient contact between particles in the early sintering stage leads to the generation of residual pores. High temperature accelerates the mass transfer process among grains. The gradual elimination of pores accompanied by grain growth effectively promotes the densification of ceramic materials.

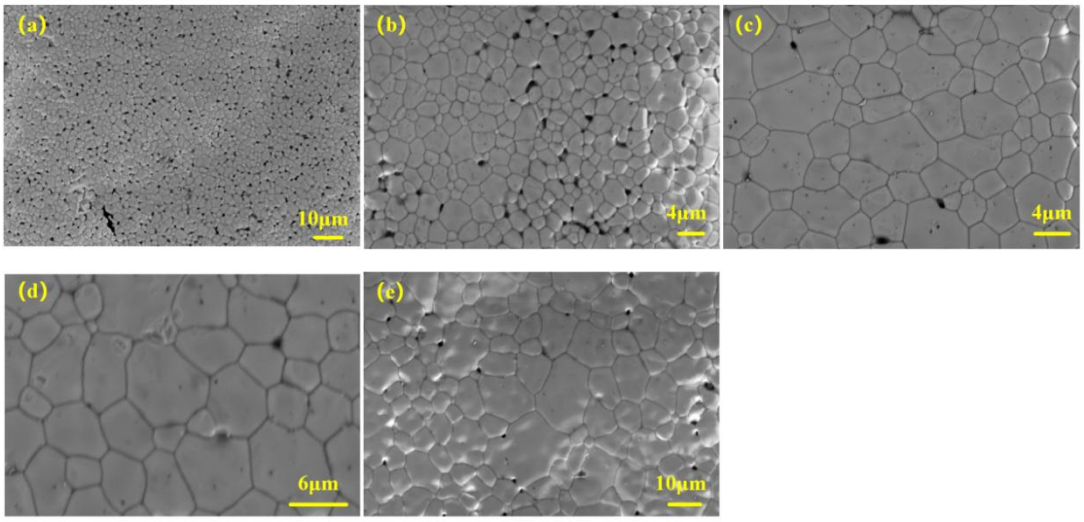


Fig. 3. $Ca_{0.92}Sr_{0.08}Sm_{1.92}Nd_{0.08}(MoO_4)_4$ ceramic surface SEM at different sintering temperature: (a) 875℃; (b) 900 ℃; (c) 925 ℃; (d) 950 ℃; (e) 975 ℃;

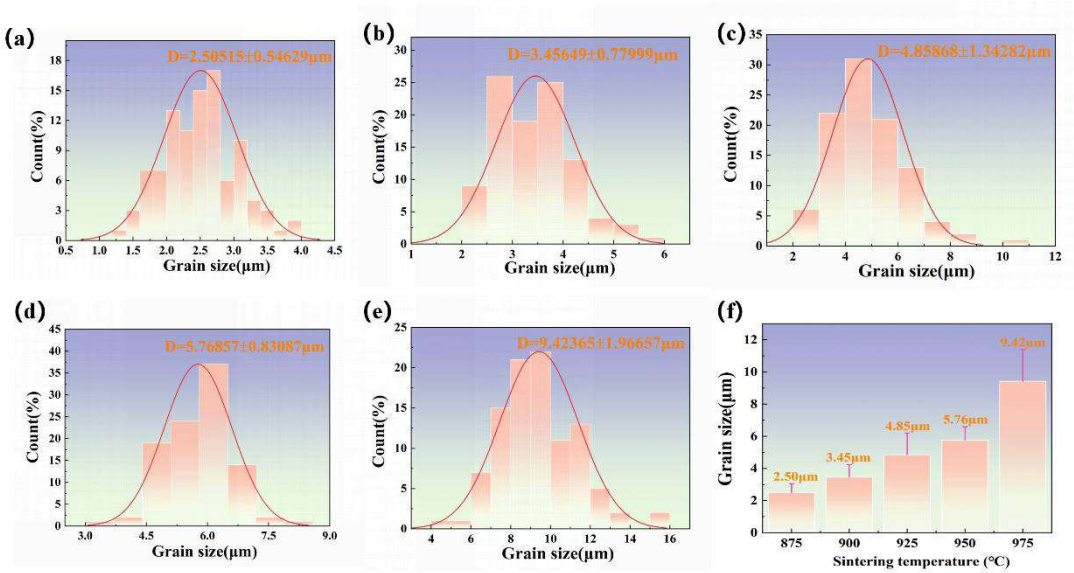


Fig. 4 Grain size distribution histograms of $Ca_{0.92}Sr_{0.08}Sm_{1.92}Nd_{0.08}(MoO_4)_4$ ceramics sintered at different temperatures: (a) 875 ℃, (b) 900 ℃, (c) 925 ℃, (d) 950 ℃, (e) 975 ℃; (f) average grain size as a function of sintering temperature ranging from 875 ℃ to 975 ℃.

According to the SEM analysis results, the bulk density and relative density curves of

$Ca_{0.92}Sr_{0.08}Sm_{1.92}Nd_{0.08}(MoO_4)_4$ ceramics sintered at different temperatures are compared in **Fig. 5(a)**. The ceramic achieves the optimal sintering state at 950℃, with a bulk density of 4.898 g/cm^3. **Fig. 5(b)** reveals that among $Ca_{1-x}Sr_xSm_{2-x}Nd_x(MoO_4)_4$ ceramics with various substitution amounts sintered at 950℃, the $Ca_{0.92}Sr_{0.08}Sm_{1.92}Nd_{0.08}(MoO_4)_4$ specimen possesses the maximum relative density of 95.96%, which is the highest among all substitution ratios. As presented in **Fig. 5(a)**, both bulk density and relative density of the ceramics first increase to a maximum value and then decline with rising sintering temperature. When the sintering temperature of $Ca_{0.92}Sr_{0.08}Sm_{1.92}Nd_{0.08}(MoO_4)_4$ ceramics exceeds the optimal temperature of 950℃, the density decreases with further increasing temperature. This phenomenon originates from the enhanced driving force for grain boundary migration at excessive temperature, which triggers abnormal grain growth. Pores are trapped inside grains and form isolated closed pores that are difficult to eliminate, leading to the reduction of relative density[25]. This observation is consistent with the SEM results. The increase in relative density can raise the number of internal dipoles and enhance polarizability, which further contributes to the improvement of permittivity.

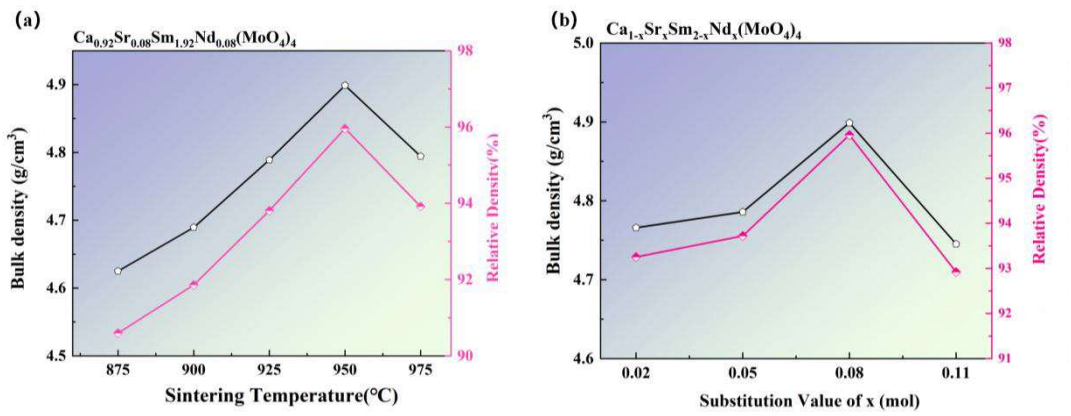


Fig. 5 Bulk density and relative density of **(a)** $Ca_{0.92}Sr_{0.08}Sm_{1.92}Nd_{0.08}(MoO_4)_4$ ceramics sintered at various temperatures and **(b)** $Ca_{1-x}Sr_xSm_{2-x}Nd_x(MoO_4)_4$ ceramics with different substitution contents of x.

According to the XRD results, $Ca_{1-x}Sr_xSm_{2-x}Nd_x(MoO_4)_4$ (x=0.02,0.05,0.08,0.11) ceramics exhibit a single-phase structure without any secondary phases. Accordingly, the influence of secondary phases on permittivity can be excluded, and the variation of ε_r is analyzed from the perspective of extrinsic factors. In general, pores are easily formed during ceramic sintering, which affect the relative permittivity and introduce experimental errors. To eliminate such errors originating from porosity, the correction formula proposed by Bosman and Havinga is adopted to calibrate the relative permittivity[26]. The corrected permittivity is expressed as:

$$\varepsilon_{corrected} = \varepsilon_r(1 + 1.5P) \quad (2)$$

where P stands for the porosity of ceramic samples. **Fig. 6** displays the dependence of corrected permittivity on substitution fraction for $Ca_{1-x}Sr_xSm_{2-x}Nd_x(MoO_4)_4$ ceramics. The polarizability can be calculated by the Clausius–Mossotti equation[27]:

$$\varepsilon_{th} = \frac{3V_m + 8\pi\alpha_T}{3V_m - 4\pi\alpha_T} \quad (3)$$

where V_m represents the unit cell volume and α is the molecular polarizability. The polarizability of the compound is typically calculatedusing the Shannon additive rule[48]:

$$\begin{aligned}&\alpha_T\left(Ca_{1-x}Sr_xSm_{2-x}Nd_x(MoO_4)\right)\\&= (1-x)\alpha(Ca^{2+}) + x\alpha(Sr^{2+}) + (2-x)\alpha(Sm^{3+}) + x\alpha(Nd^{3+})\\&+4\alpha(Mo^{6+}) + 16\alpha(0^{2-})\end{aligned} \quad (4)$$

The polarizability values are 3.16 for Ca^{2+}, 4.24 for Sr^{2+}, 4.74 for Sm^{3+}, 5.01 for Nd^{3+}, 3.28 for Mo^{6+}, and 2.01 for O^{2-}. Both the theoretical permittivity (ε_r,theo) and the density-corrected permittivity (ε_r,corr) decrease monotonically with increasing x and are fully consistent in their variation tendency. Although the co-substitution of Sr^{2+} and Nd^{3+}-which possess larger ionic polarizabilities than the Ca^{2+} and Sm^{3+} ions they replace-is intended to raise the total polarizability, it simultaneously enlarges the unit-cell volume. Evaluation based on the Clausius–Mossotti equation reveals that the volume-dilution effect overcomes the increase in polarizability, so that the theoretical permittivity of the ceramics decreases with x. Accordingly, the measured permittivity is predominantly governed by the extrinsic factor of relative density, which reasonably accounts for the close correlation between the permittivity and the relative density observed across the series.

The measured ionic polarizability (P_{mea}) is obtained from experimental ε_r values, while the theoretical ionic polarizability (P_{theo}) is determined based on the additive rule. On this basis, the theoretical permittivity (ε_r,theo) of $Ca_{1-x}Sr_xSm_{2-x}Nd_x(MoO_4)_4$(x=0.08) ceramics is calculated to be 10.47, slightly lower than the measured value. Relative permittivity is affected by multiple factors. Although the results derived from the above equations provide valuable references, they should not be regarded as the sole evaluation criterion. Zhao *et al.* also reported a relatively low permittivity for $CaSm_2(MoO_4)_4$ ceramics[16]. Therefore, it can be concluded that relative density is the dominant factor affecting the relative permittivity of $Ca_{1-x}Sr_xSm_{2-x}Nd_x(MoO_4)_4$ ceramics.

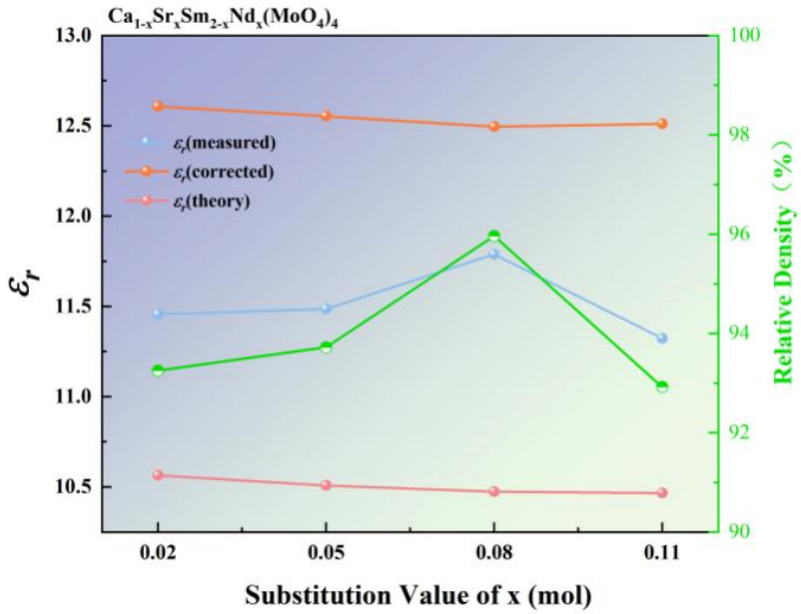


Fig. 6 relationship between the theoretical and measured dielectric constants and relative density of $Ca_{1-x}Sr_xSm_{2-x}Nd_x(MoO_4)_4$ ceramics.

Raman spectroscopy is an effective technique to investigate the evolution of crystal structure, cation arrangement, phase composition, and the structure-property relationship in various systems [28]. Based on the above analysis, it can be concluded that $Ca_{0.92}Sr_{0.08}Sm_{1.92}Nd_{0.08}(MoO_4)_4$ ceramic exhibits optimal densification performance. In order to explore the correlation between its Raman spectral characteristics and dielectric properties, room-temperature Raman tests and analyses were performed on $Ca_{0.92}Sr_{0.08}Sm_{1.92}Nd_{0.08}(MoO_4)_4$ samples. The Raman spectra of these ceramics recorded in the range of 150 ~ 1000 cm^{-1} are presented in **Fig. 7**. Combined with the XRD results, $Ca_{1-x}Sr_xSm_{2-x}Nd_x(MoO_4)_4$ ceramics possess a tetragonal scheelite-type structure with the space group $I4_1/a$ and point group C4h(4/m). According to group theory analysis, at the Brillouin zone center, the structure with the C4h point group contains 26 distinct vibration modes[29]:

$$T=3A_g+5A_u+5B_g+5B_u+5E_g+5E_u \quad (5)$$

Among them, only A_g, B_g, and E_g modes correspond to Raman-active vibrations. Hence, 13 Raman-active modes are expected at the Brillouin zone center for $Ca_{1-x}Sr_xSm_{2-x}Nd_x(MoO_4)_4$ ceramics. Only seven Raman bands were observed in the measured wavenumber range. The remaining vibrational modes were not resolved, owing to their relatively weak intensities and mutual overlap with the characteristic bands. In the $Ca_{1-x}Sr_xSm_{2-x}Nd_x(MoO_4)_4$ structure, lattice vibration modes can be divided into internal and external modes. The external modes (below 300

cm^{-1}) originate from the translational and rotational motions of Ca^{2+} and Sm^{3+} ions. The internal modes (above 300 cm^{-1}) are assigned to vibrations within the [MoO_4] clusters, including symmetric bending vibration v_2 (at 314cm^{-1}), asymmetric bending vibration v_4 (315–450cm^{-1}), asymmetric stretching vibration v_3 (600–850 cm^{-1}), and symmetric stretching vibration v_1 (at 898 cm^{-1}). The strongest peak is attributed to the symmetric stretching vibration of [MoO_4] tetrahedra, which belongs to the A_g mode[16].

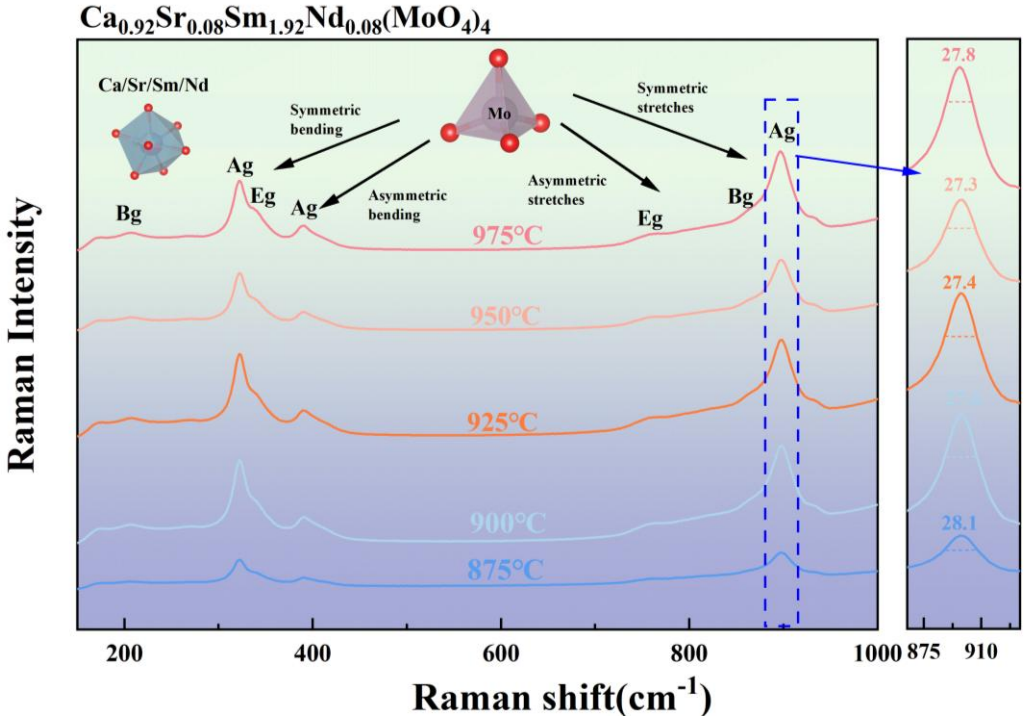


Fig. 7 Raman spectra of $Ca_{0.92}Sr_{0.08}Sm_{1.92}Nd_{0.08}(MoO_4)_4$ ceramics sintered at various temperatures.

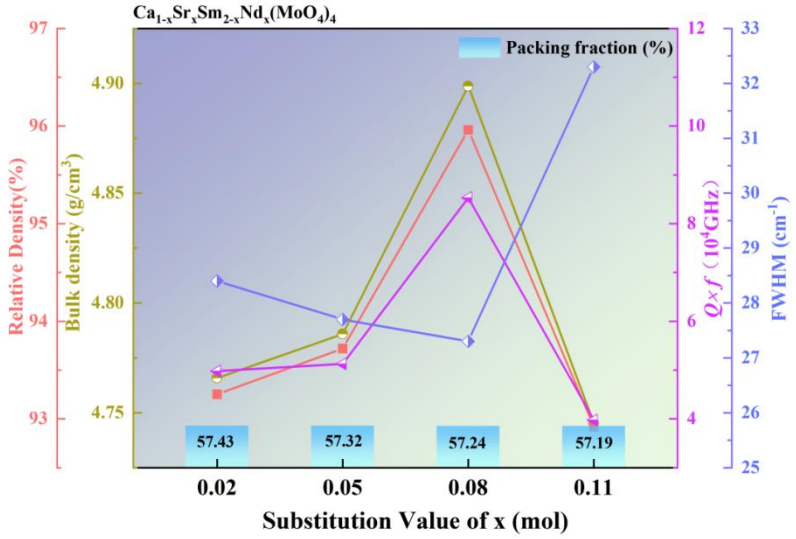


Fig. 8 Q×f, Raman half-width, relative density, actual density, packing fraction relationship diagram of $Ca_{1-x}Sr_xSm_{2-x}Nd_x(MoO_4)_4$ ceramics.

Numerous experimental and theoretical results[30-33] demonstrate that a smaller full width at half maximum (FWHM) of Raman peak corresponds to a higher Q×f value. This is because the damping effect of the vibration mode at 898 cm^{-1} weakens with the decrease of FWHM, which reduces the intrinsic dielectric loss of the material[31]. **Fig. 8** presents the FWHM of the Raman peak located at 898 cm^{-1}, which can characterize the cation ordering degree. An obvious inverse correlation between FWHM and Q×f with the variation of relative density can be observed. When the FWHM reaches its minimum value of 27.3 cm^{-1}, the Q×f value is 85,324 GHz. Accordingly, the cation ordering degree can effectively characterize the evolution of the Q×f value for $Ca_{0.92}Sr_{0.08}Sm_{1.92}Nd_{0.08}(MoO_4)_4$ ceramics.

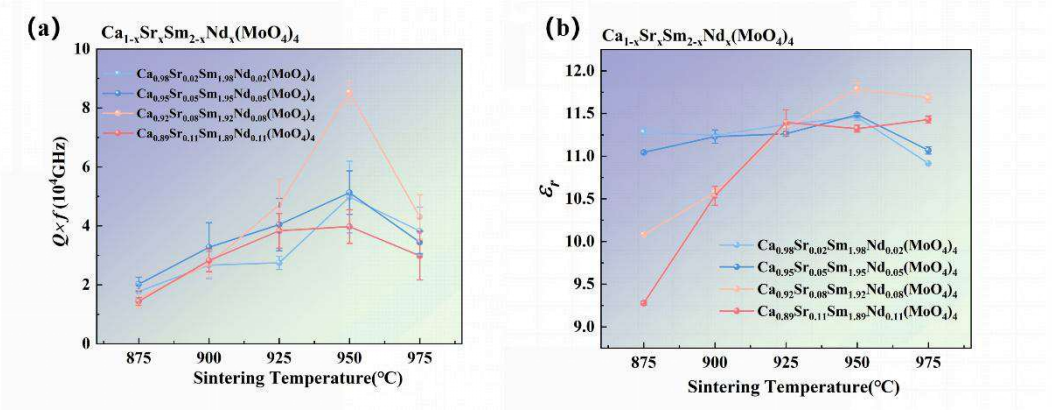


Fig. 9 (a) the Q×f values and **(b)** relative permittivity ε_r of $Ca_{0.92}Sr_{0.08}Sm_{1.92}Nd_{0.08}(MoO_4)_4$ ceramics sintered at different temperatures.

In general, the Q×f factor of dielectric ceramics is determined by extrinsic and intrinsic factors. As discussed above, secondary phases exert negligible influence on Q×f. Relative density acts as the dominant extrinsic factor: higher relative density leads to a larger Q×f value. This work systematically investigates how intrinsic factors including packing fraction and lattice vibration regulate the Q×f values and ε_r of $Ca_{1-x}Sr_xSm_{2-x}Nd_x(MoO_4)_4$ (x = 0.02, 0.05, 0.08, 0.11) ceramics sintered at diverse temperatures, as illustrated in **Fig. 9(a-b)**. Combined with spectrum diagrams, SEM morphologies and density curves, the ceramics achieve optimal dielectric properties at the optimal sintering temperature of 950 °C. Accordingly, **Fig. 8** offers comparative analysis for samples with various substitution ratios sintered uniformly at 950℃. Sharp decline in relative density brings about obvious deterioration in Q×f, which strongly proves the vital role of densification[34-35]. Moreover, the consistent variation tendency between FWHM and Q×f further confirms the reliability of experimental results. Although the packing fraction gradually declines, its variation range is limited. Consequently, ceramic densification is identified as the decisive factor

for Q×f, while packing fraction only plays a minor role.

$$P.F.(\%) = \frac{\text{Volume of packed ions}}{\text{Volume of unit cell}} \times Z \tag{6}$$

The parameter Z denotes the number of formula units within a unit cell.

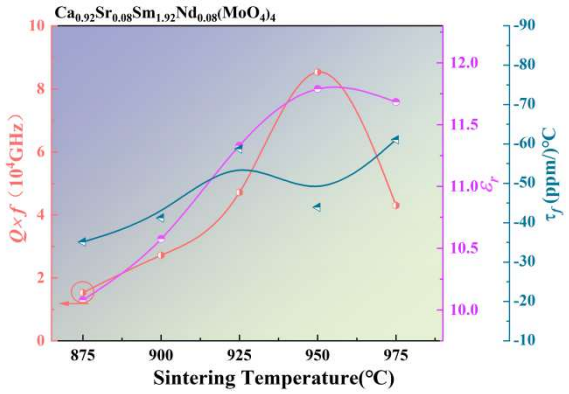


Fig. 10 dielectric properties of $Ca_{0.92}Sr_{0.08}Sm_{1.92}Nd_{0.08}(MoO_4)_4$ ceramics at different temperatures.

Fig. 10 illustrates the dielectric properties of $Ca_{0.92}Sr_{0.08}Sm_{1.92}Nd_{0.08}(MoO_4)_4$ ceramics sintered at different temperatures. It can be clearly observed that all obtained τ_f values are small negative values ranging from −30 to −60 ppm/°C. The τ_f value varies slightly with sintering temperature, revealing that the sintering temperature exerts a negligible influence on the τ_f of the ceramic.

It is well known that the P-V-L chemical bond theory is widely used to explore the relationship between microwave properties and chemical bond characteristics, laying a foundation for investigating the chemical bonding features of microwave dielectric ceramics[36-37]. Based on the decomposed chemical formula, the ionicity, lattice energy, bond energy and thermal expansion coefficient of chemical bonds can be further calculated and analyzed, which helps reveal the influences of chemical bond evolution on the crystal structure as well as the dielectric properties of microwave dielectric ceramics[36]. Therefore, combined with the optimized parameters and P-V-L chemical bond theory, bond parameters including bond ionicity (f_i), lattice energy U, bond energy E and thermal expansion coefficient (α) were calculated in this work. Detailed calculation procedures can be found in previous literatures[37-40], and the main calculation formulas are displayed as follows:

$$f_i = \frac{\left\{14.4bexp(-k_s/2)\left[\frac{Z_A^*}{r_0} - (n/m)\frac{Z_B^*}{r_0}\right]\right\}^2}{E_h^2 + C^2} \tag{7}$$

where m and n denote the number of atoms of the cation A and the anion B in the sub-formula m and n respectively, f_i is the individual bond ionicity of bond μ. E_g^u and C^μ are the average

energy gap and ionic energy gap, respectively. d^{μ} represent the bond length, b^{μ} is the correction factor. r_{μ}^{0} is the average radius of binary A_mB_n. $\left(Z_A^{\mu}\right)^*$ and $\left(Z_B^{\mu}\right)^*$ are the effective number of valence electrons.

$$U_{cal} = \sum\nolimits_{\mu} \left(U_{bc}^{\mu} + U_{bi}^{\mu}\right) \tag{8}$$

$$U_{bc}^{\mu} = 2100m \frac{\left(Z_{+}^{\mu}\right)^{1.64}}{\left(d^{\mu}\right)^{0.75}} f_c^{\mu} \tag{9}$$

$$U_{bi}^{\mu} = 1270 \frac{(m+n) Z_{+}^{\mu} Z_{-}^{\mu}}{d^{\mu}} \left(1 - \frac{0.4}{d^{\mu}}\right) f_i^{\mu} \tag{10}$$

Where U_{cal} denotes the overall lattice energy, and U_{bc} and U_{bi} correspond to the covalent component and ionic component, respectively.

$$\alpha = \sum F_{mn}\, \alpha_{mn} \tag{11}$$

$$\alpha_{mn} = -3.0685 + 0.8376\gamma_{mn} \tag{12}$$

$$\gamma_{mn} = \frac{kZ_A N_{CA}}{U\Delta_A} \beta_{mn} \tag{13}$$

$$\beta_{mn} = \frac{m(m+n)}{2n} \tag{14}$$

where F_{mn} is the fraction of the calculated chemical bond among all chemical bonds, *k* is the Boltzmann constant, *U* denotes the lattice energy of the above chemical bond, and Δ represents the periodic constant of cations.

$$E = t_i \frac{33200}{d} + t_c \frac{(r_{cA} + r_{cB})}{d} \left(E_{A-A} E_{B-B}\right)^{0.5} \tag{15}$$

where r_{cA} and r_{cB} correspond to the covalent radii of elements A and B. t_c and t_i refer to covalent and ionic blending coefficients, while E_{A-A} and E_{B-B} are homonuclear bond energies.

$$\begin{gathered} Ca_{1-x}Sr_xSm_{2-x}Nd_{2x}(MoO_4)_3 \\ \rightarrow (Ca_{1-x}Sr_xSm_{2-x}Nd_{2x})_{1/3}MoO_4 = AMoO_4 = AO_{8/3}MoO_{4/3} \\ \rightarrow A_{1/2}O(1)_{4/3} + A_{1/2}O(2)_{4/3} + MoO_{4/3} \end{gathered} \tag{16}$$

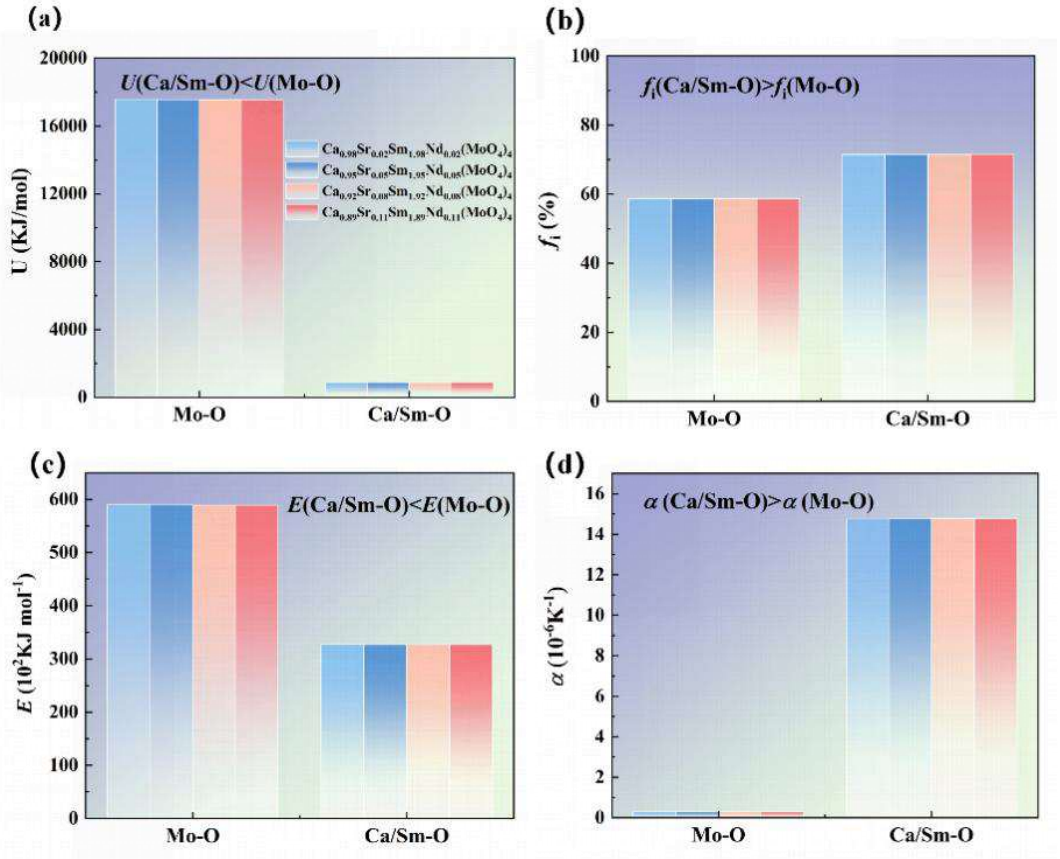


Fig. 11 (a) lattice energy of $Ca_{1-x}Sr_xSm_{2-x}Nd_x(MoO_4)_4$ ceramics; **(b)** ionicity of $Ca_{1-x}Sr_xSm_{2-x}Nd_x(MoO_4)_4$ ceramics; **(c)** bond energy of $Ca_{1-x}Sr_xSm_{2-x}Nd_x(MoO_4)_4$ ceramics; **(d)** thermal expansion coefficient of $Ca_{1-x}Sr_xSm_{2-x}Nd_x(MoO_4)_4$ ceramics.

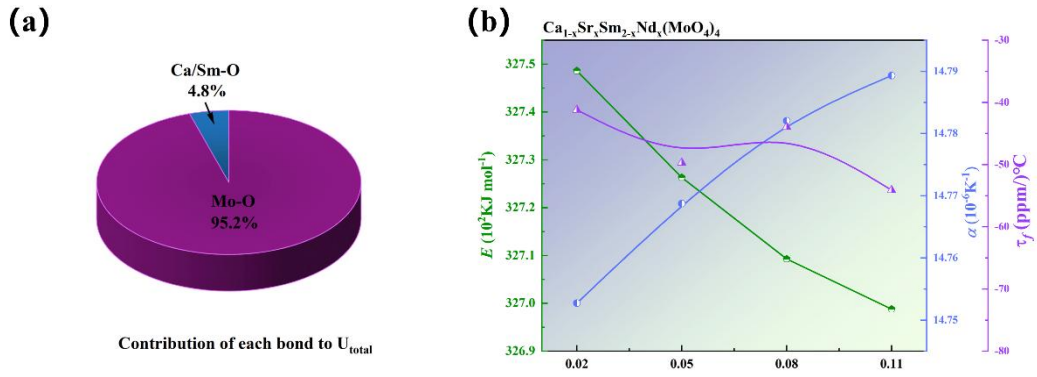


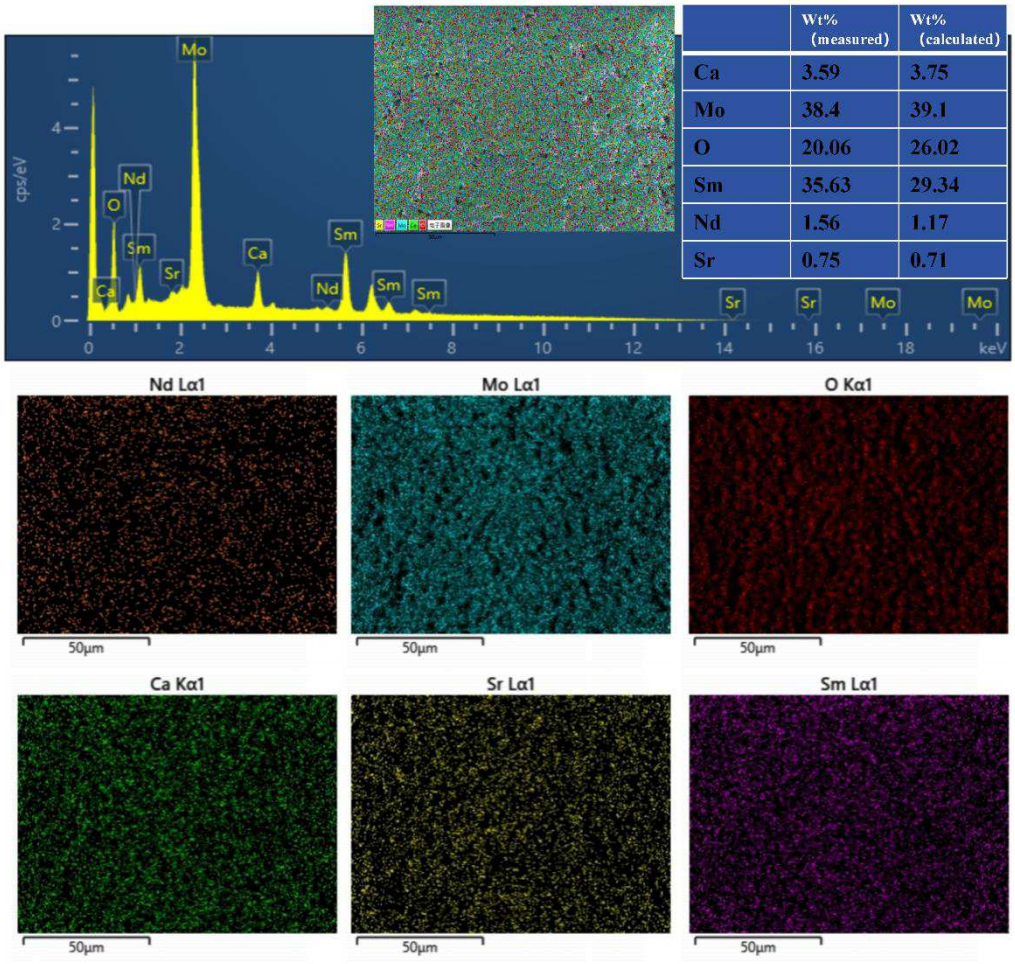
Fig. 12 (a) Contributions of the Mo–O and Ca/Sm–O bonds to the total lattice energy (U_{total}) of the $Ca_{1-x}Sr_xSm_{2-x}Nd_x(MoO_4)_4$ ceramics; **(b)** the bond energy (E) of the Ca/Sm–O bond together with the thermal expansion coefficient (α) and the bond-related temperature coefficient (τ_f) of the Mo–O bond as functions of the substitution content x.

The P–V–L bond analysis of this scheelite-type structure shows that the Ca/Sm–O bonds possess the highest ionicity among the constituent bonds, which underlies their dominant contribution to the relative permittivity as illustrated in **Fig. 11(b)**, whereas the Mo–O bonds exhibit the largest lattice and bond energies, reflecting the strong Mo–O bonding that stabilizes the framework and is associated with the low intrinsic loss of this system as illustrated in **Fig. 11(a) and Fig. 12(a)**. Within the narrow compositional window studied, the bond parameters (ionicity, lattice energy and bond energy) vary only slightly with x; they are therefore presented here as descriptors of the chemical-bonding evolution rather than as the factors governing the compositional trends of Q×f and εr.

The coefficient of thermal expansion α is another important parameter influencing τf values. Mo-O bonds play a dominant role in influencing α values as demonstrated in **Fig. 11(d)**. Accordingly, the correlation between τf and $\alpha_{A(Mo\text{-}O)}$ is explored and shown in **Fig. 12(b)**. τf is inversely proportional to $\alpha_{A(Mo\text{-}O)}$ as x values increase. This discovery can be reasonably explained by showing a relation between τf, the thermal expansion coefficient(a)and the temperature coefficient ofthe dielectric constant (τ_ε) :

$$\tau_f = -\alpha - (1/2)\tau_\varepsilon \tag{17}$$

The thermal expansion coefficient α derived from the P–V–L theory varies with x in accordance with the evolution of τf from −53 ppm/°C for the parent composition to −43.94 ppm/°C at x = 0.08, i.e., toward a smaller negative value and hence an improved temperature stability.



	Wt% (measured)	Wt% (calculated)
Ca	3.59	3.75
Mo	38.4	39.1
O	20.06	26.02
Sm	35.63	29.34
Nd	1.56	1.17
Sr	0.75	0.71

Fig. 13 EDS spectrum, quantitative composition, and elemental mappings of the $Ca_{0.92}Sr_{0.08}Sm_{1.92}Nd_{0.08}(MoO_4)_4$ ceramic, confirming the homogeneous distribution of Ca, Sr, Sm, Nd, Mo and O.

Energy-dispersive X-ray spectroscopy (EDS) elemental mapping and line-scan analyses were performed on the polished surface of the x = 0.08 ceramic as illustrated in **Fig. 13 and 14**. The mapping images reveal that Ca, Sr, Sm, Nd, Mo and O are uniformly distributed across the examined region without elemental segregation, and the measured cation ratios are in semiquantitative agreement, within the accuracy of EDS, with the nominal $Ca_{0.92}Sr_{0.08}Sm_{1.92}Nd_{0.08}(MoO_4)_4$ stoichiometry.

To evaluate the chemical compatibility of the ceramic with Ag electrodes for LTCC application, the $Ca_{0.92}Sr_{0.08}Sm_{1.92}Nd_{0.08}(MoO_4)_4$ ceramic was co-fired with Ag paste at 950°C. **Fig. 14** presents the cross-sectional SEM image and the corresponding EDS line-scan profiles across the Ag/ceramic interface. A dense, continuous and well-bonded Ag layer is formed on the ceramic substrate, with a

distinct and crack-free interface. The EDS line scans of O, Ca, Sm, Mo and Ag reveal a sharp elemental transition at the interface: the Ag signal is confined to the electrode region, whereas O, Ca, Sm and Mo are distributed only in the ceramic region, without detectable interdiffusion or elemental enrichment at the boundary. The absence of a distinct interfacial diffusion layer indicates that the ceramic and the Ag electrode do not react with each other during co-firing, demonstrating good chemical compatibility. This favourable compatibility, together with the low sintering temperature, makes the $Ca_{0.92}Sr_{0.08}Sm_{1.92}Nd_{0.08}(MoO_4)_4$ ceramic a promising candidate for Ag-based LTCC applications.

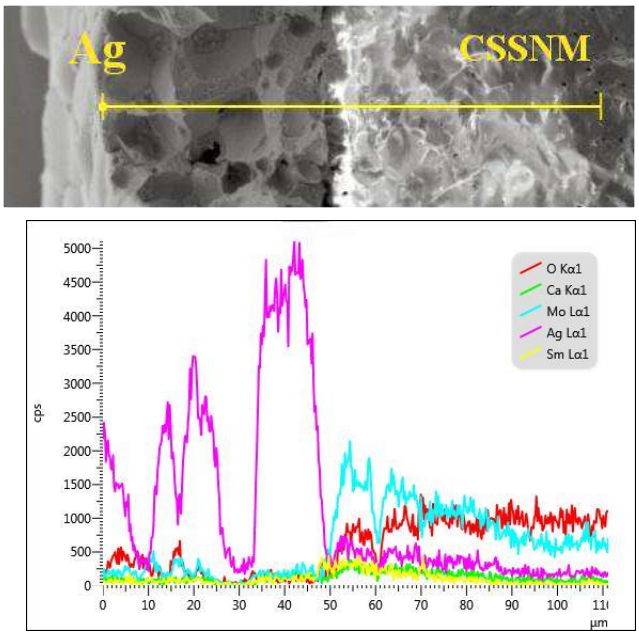


Fig. 14 Cross-sectional SEM image and EDS line-scan analysis of the $Ca_{0.92}Sr_{0.08}Sm_{1.92}Nd_{0.08}(MoO_4)_4$ ceramic co-fired with Ag at 950°C, showing a well-bonded interface without significant interdiffusion between the Ag electrode and the ceramic.

Conclusion

In this study, a series of $Ca_{1-x}Sr_xSm_{2-x}Nd_x(MoO_4)_4$ ceramics were synthesized via the conventional solid-state reaction method. The Sr^{2+}/Nd^{3+} co-substitution maintains a single-phase tetragonal scheelite-type solid solution without secondary phases and lowers the optimum sintering temperature from 1000 °C for the parent to 950 °C. The $Ca_{0.92}Sr_{0.08}Sm_{1.92}Nd_{0.08}(MoO_4)_4$ ceramic sintered at 950 °C attains a high relative density of 95.96% and optimal microwave dielectric properties of εr = 11.788, Q×f = 85,324 GHz and τf = -43.94 ppm/°C. The improvement in Q×f is attributed mainly to enhanced densification, which suppresses porosity-related loss, together with a

genuine intrinsic contribution from improved cation ordering, as revealed by the narrowing of the Raman FWHM. The relative permittivity decreases slightly with increasing x, governed primarily by the expansion of the unit cell that dilutes the polarizability density, and is further modulated by the relative density. According to the P–V–L bond theory, the Ca/Sm–O bonds exhibit the highest ionicity and thus dominate the permittivity contribution, whereas the strong Mo–O bonds, possessing the largest lattice and bond energies, stabilize the crystal framework; the derived thermal expansion coefficient α correlates with the temperature stability of τf. All samples exhibit moderate negative τf values of -30 to -60 ppm/°C. The combination of low-temperature sinterability and high Q×f renders this series a promising candidate for LTCC applications.

Acknowledgments

This study was financially supported by the Zhaoqing University Research Fund (Nos. 202601260406 and 2026012146) and Guangdong Province Postgraduate Education Innovation Plan Funding Project.

Reference

[1]W. Guo, Z. Ma, Y. Luo, Y. Chen, Z. Yue, L. Li, Structure, defects, and microwavedielectric properties of Al-doped and Al/Nd co-doped $Ba_4Nd_{9.33}Ti_{18}O_{54}$ ceramics, J. Adv. Ceram. 11(2022)629-640.

[2]M. Cao, L. Li, S. Y. Wu, X. M. Chen, Dominant role of ceramic connectivity in microwave dielectric properties of porous ceramics, Acta Mater. 258(2023)119207.

[3]TAN K, SONG T, SHEN T, et al. Research progress of microwave dielectric ceramics with low dielectric constant, J. Adv. Ceram, 43 (2022) 11-29.

[4]HU J, LV XP, ZHANG J, et al. Research progress of microwave dielectric ceramics[J]. Inf. Rec. Mater, 19 (2018) 6-8.

[5]WANG MZ. 5G mobile communication development trend and key technology research[J]. Wisdom China 02 (2022) 68-69.

[6]D. Zhou, L-X. Pang, D.-W. Wang, Z.-M. Qi, I. M. Reaney, High quality factor, ultra low sintering temperature $Li_6B_4O_9$ microwave dielectric ceramics with ultra low density for antenna substrates,ACS Sustain. Chem. Eng. 6(2018)11138-11143.

[7]W. B. Hong, L. Li, H. Yan, S. Y. Wu, H. S. Yang, X. M. Chen, Room-temperature-densified H_3BO_3 microwave dielectric ceramics with ultra-low permittivity andultra-high Qf value, J. Materiomics 6(2020)233-239.

[8]W. Wang, J. Bao, C. Wang, G. He, X. Wang, D. Xu, B. Jin, Z. Shi, M. A. Darwish, Y. Chen, Q. Liang, M. Zhang, D. Zhou, $LiMSiO_4$(M=Ga,Sc and Y): low-Permittivity and high thermal conductivity microwave dielectric ceramics for millimeter-wave communications, J. Mater. Sci. Technol. 225(2025)288-296.

[9]T. Shi, J. Zhu, Microwave dielectric properties and microstructure of a new kind Eu-based $Eu(Mg_{0.5}Ti_{0.5})O_3$ ceramic, Rare Met. 37 (2018) 913-918.

[10]X.-Q. Song, M.-Q. Xie, K. Du, W.-Z. Lu, W. Lei, Synthesis, crystal structure and microwave dielectric properties of self-temperature stable $Ba_{1-x}Sr_xCuSi_2O_6$ ceramics for millimeter-wave communication, J. Materiomics 5 (2019) 606-617.

[11]J. Bao, K.-H. Zhang, W. Wang, Z.-Y. Liu, Z. Fang, X. Wang, C.-H. Wang, Y.-C. Li, G.-Q. He, T. Zhou, D. Zhou, A series of ultra-low permittivity $ALaP_4O_{12}$(A = Li, Na, K) metaphosphate microwave dielectric ceramics for ultra-wideband dielectricresonant antenna application, ACS Appl. Mater. Interfaces 16 (2024)58898-58911.

[12]X.Q. Song, K. Du, Z.Y. Zou, Z.H. Chen, W.Z. Lu, S.H. Wang, W. Lei, Temperaturestable BaAl2Si2O8 – Ba5Si8O21-based low-permittivity microwave dielectric ceramics for LTCC applications, Ceram. Int. 43 (2017) 14453 – 14456.

[13]J. Zhou, Towards rational design of low-temperature co-fired ceramic (LTCC) materials. J. Adv. Ceram. 1(2), (2012) 89-99.

[14]J. Ren, K. Bi, X. Fu, Z. Peng, Novel $Al_2Mo_3O_{12}$-based temperature-stable microwave dielectric ceramics for LTCC applications, J. Mater. Chem. C 6 (2018) 11465–11470.

[15]Y.C. Lee, J.D. Chiu, Y.H. Chen, Effects of Nb_2O_5 doping on the microwave dielectric properties and microstructures of $Bi_2Mo_2O_9$ ceramics, J. Am. Cerm. Soc 96 (2013) 1477–1482.

[16]Ziqi Zhao, Xiaoli Wei, Wenjie Zhang, Yuan Nie, Yanjun Liu, Fangyi Huang, Huanfu Zhou, Crystal structure, sintering behavior, and microwave dielectric properties of CaSm2(MoO4)4 ceramics for millimeter-wave communication, Ceram. Int. 51 (2025) 38591-38598.

[17]M. Yu, Y. Tang, J. Li, W. Fang, L. Duan, L. Fang, Microwave dielectric properties and chemical compatibility with alumina electrode of two novel ultra-low temperature firing $ATeMoO_6$ (A = Mg, Zn) ceramics, Ceram. Int. 46 (2020) 25619–25625.

[18]X. Wei, Y. He, X. Chen, H. Zhou, Phase composition, Raman spectrum and microwave dielectric properties of glass-free low temperature co-fired $ACaPr(MoO_4)_3$ (A = Na, K) ceramics, Ceram. Int. 49 (2023) 36962–36969.

[19]H.-H. Xi, D. Zhou, H.-D. Xie, W.-B. Li, Microwave dielectric properties of low firing $(Na_{0.5}Ln_{0.5})MoO_4$ (Ln=Nd and Ce) ceramics, Ceram. Int. 41 (2015) 6103-6107.

[20]Meiying Li, Binghong Huang, Fei Shang , Guohua Chen A novel dielectric ceramic $Na_{0.48}La_{0.52}MoO_4$ with excellent thermal stability for LTCC applications, Ceram. Int. 50 (2024) 13544-13549.

[21]K. Liu, X. Wang, P. Gao, X. Wei, Y. Xiao, S. Deng, X. Qu, G. He, Q. Li, L. Deng,X. Chen, H. Zhou, Novel $CaLn_4Mo_3O_{16}$(Ln=La, Nd, and Sm) ceramics: sintering behaviour, phase structure and microwave dielectric performance, Ceram. Int. 48 (2022) 27360-27368.

[22]G. K. Choi, J. R. Kim, S. H. Yoon, K. S. Hong, Microwave dielectric properties of scheelite (A=Ca, Sr, Ba) and wolframite (A=Mg,Zn, Mn) $AMoO_4$ compounds, J. Eur. Ceram. Soc. 27 (2007) 3063-3067.

[23]D. Zhou, L.-X. Pang, J. Guo, Y. Wu, G.-Q. Zhang, W. Dai, H. Wang, X. Yao, Newmicrowave dielectric ceramics $BaLn_2(MoO_4)_4$ (Ln = Nd and Sm) with low loss, J. Am. Ceram. Soc. 94 (2011) 2800-2803.

[24]B.W. Hakki, P.D. Coleman, A dielectric resonator method of measuring inductive capacities in the millimeter range, IRE Trans. Microw. Theory Tech. 8 (1960) 402–410.

[25]P. Gao, K. Liu, X. Wei, X. Qu, S. Deng, Y. Xiao, J. Yang, Y. Wu, X. Chen, H. Zhou, NaYW2O8: a novel glass-free microwave dielectric ceramic for LTCC application, Ceram. Int. 49 (2023) 23165-23172.

[26]A. J. Bosman, E. E. Havinga, Temperature dependence of dielectric constants of cubic ionic compounds, Phys. Rev.129 (1963) 1593-1600.

[27]Y. Wu, D. Zhou, J. Guo, L.X. Pang, H. Wang, X. Yao, Temperature stable microwave dielectric ceramic $0.3Li_2TiO_3$-$0.7Li(Zn_{0.5}Ti_{1.5})O_4$ with ultra-low dielectric loss, Mater. Lett. 65 (2011) 2680-2682.

[28]D.L. Rousseau, R.P. Bauman, S.P.S. Porto, Normal mode determination in crystals, J. Raman Spectrosc. 10 (1) (1981) 253–290.

[29]V. S. Marques, LS. Cavalcante, J. C. Sczancoski, A. F. P. Alcantara, M. O. Orlandi, E. Moraes, E. Longo, J. A. Varela, M. Siu Li, M. R. M. C. Santos, Effect of different solvent ratios (Water/Ethylene glycol) on the growth process of $CaMoO_4$ crystalsand their optical properties, Cryst. Growth Des. 10 (2010) 4752-4768.

[30]Z. Yang, Y. Tang, J. Li, W. Fang, J. Ma, A. Yang, L. Liu, L. Fang, Crystal structure, Raman spectra and microwave dielectric properties of novel low-temperature cofired ceramic Li_4GeO_4, J. Alloy. Compd. 867 (2021) 159059.

[31]S.M. Wan, S.J. Zhang, X.Y. Going, Y. Zeng, S.J. Jiang, J.L. You, Structural in vestigations on two typical lithium germanate melts by in situ Raman spec troscopy and density functional theory calculations, Cryst. Eng. Comm. 22 (2020) 701-707.

[32]S.K. Singh, V.R.K. Murthy, Microwave dielectric properties of Li2SrTa2(1−x)Nb2xO7 ceramics investigated by Raman spectroscopy, Ceram. Inter. 42 (2016) 7284-7289.

[33]S.H. Yoon, D.W. Kim, S.Y. Cho, K.S. Hong, Investigation of the relations between structure and microwave dielectric properties of divalent metal tungstate compounds, J. Eur. Ceram. Soc. 26 (2006) 2051-2054.

[34]C. Xing, J. Li, H. Chen, H. Qiao, J. Yang, H. Dong, H. Sun, J. Wang, X. Yin, Z.-M. Qi,F. Shi, Phonon characteristics, crystal structure, and intrinsic properties of a $Y(Mg_{1/2}Sn_{1/2})O_3$ ceramic, RSC Adv. 7 (56) (2017) 35305–35310.

[35]X. Chen, H. Li, P. Zhang, G. Li, Microwave dielectric properties of $Co_2P_2O_7$ceramics, Ceram. Int. 47 (2) (2021) 1980–1985.

[36]Yuan-Bin Chen, Siyi Xiong,Structural characteristics, P-V-L theory, Raman spectra, and microwave dielectric properties of $(La_{1-x}Nd_x)_2(Zr_{0.96}Ti_{0.04})_3(MoO_4)_9$ ceramics for LTCC applications,J. Eur. Ceram. Soc. 45 (2025) 116974.

[37]Z.J. Wu, S.Y. Zhang, Calculation of chemical bond parameters in $La_{1-x}Ca_xCrO_3$ ($0.0\leq x\leq 0.3$), Int. J. Quant. Chem. 73 (1999) 433–437.

[38]Q.B. Meng, Z.J. Wu, S.Y. Zhang, The bond ionicity in $RBa_2Cu_3O_7$ (R = Pr, Sm, Eu, Gd, Dy, Y, Ho, Er, Tm), J. Phys. Condens. Matter 10 (1998) L85.

[39]Z.J. Wu, Q.B. Meng, S.Y. Zhang, Semiempirical study on the valences of Cu and bond covalency in $Y_{1-x}Ca_xBa_2Cu_3O_6$+y, Phys. Rev. B 58 (1998) 958–962.

[40]H. Yang, S. Zhang, H. Yang, E. Li, Usage of P–V–L bond theory in studying the structural/property regulation of microwave dielectric ceramics: a review, Inorg. Chem. Front. 7 (2020) 4711–4753.

[41]S.M. Zhai, P. Liu, Microwave dielectric properties of rock-salt structured $Li_7(Nb_{1-x}Ti_x)_2O_8$-xF ($0\leq x\leq 0.10$) system with low sintering temperature. Ceram. Int. 48, (2022) 28268–28273.

[42]X.Q. Song, W.Z. Lu, Y.H. Lou, T. Chen, S.W. Ta, Z.X. Fu, W. Lei, Synthesis, lattice energy and microwave dielectric properties of $BaCu_{2-x}Co_xSi_2O_7$ ceramics. J. Eur. Ceram. Soc.40, (2020) 3035–3041.

[43]R.T. Sanderson, Electronegativity and bond energy, J. Am. Chem. Soc. 105 (8) (1983) 2259–2261.

[44]R.T. Sanderson, Multiple and single bond energies in inorganic molecules, J. Inorg. Nucl. Chem. 30 (2) (1968) 375–393.

[45]Y.-R. Luo. Comprehensive Handbook of Chemical Bond Energies, 1st ed., CRC Press, 2007.

[46]J. Bao, H. Li, X. Xu, W. Guo, Y. Chen, Y. Zhang, J. Du, H. Wu, G. Duan, Z. Yue, Crystal structure, Raman spectrum, bond characteristics, and terahertz timedomain spectrum of novel $Na_5Tm(MoO_4)_4$ microwave dielectric ceramic with ultra-low sintering temperature and high quality factor, J. Alloy. Compd. 939 (2023) 168652.

[47]Z. Feng, X. Xu, J. Du, P. Gong, Y. Zhang, H. Wu, G. Duan, Effect of adding Sn^{4+} on crystal structure, sintering behaviors, and microwave dielectric properties of $La_2Zr_3(MoO_4)_9$ ceramics, Ceram. Int. 49 (15) (2023) 26147–26153.

[48]R.D. Shannon, Dielectric polarizabilities of ions in oxides and fluorides J. ApplPhys.73(1993)348-366.